Research Square

Preprints are preliminary reports that have not undergone peer review.
They should not be considered conclusive, used to inform clinical practice,
or referenced by the media as validated information.

Aluminum-modified silica achieves efficient removal of low fluoride wastewater by inducing crystallization

Shida Zhang
Shandong Jianzhu University
Zhen Qi
Shandong Jianzhu University
Fengke Dou
Shandong Coal Field Geological Survey and Research Institute
Weijie Zhong
Shandong Coal Field Geological Survey and Research Institute
Yingqiang Li
Shandong Jianzhu University
Zheyu Wang
Shandong Jianzhu University
Cui Zhen Sun
Shandong Jianzhu University
Feiyong Chen
Shandong Jianzhu University
Xue Shen
shenxue39@aliyun.com
Shandong Jianzhu University
Rupeng Liu
Shandong Jianzhu University

Research Article

Keywords: Seed crystal, Fluoride removal, Induced crystallization, Aluminum modification, Response surface method

Posted Date: June 11th, 2026

DOI: https://doi.org/10.21203/rs.3.rs-9785767/v1

License: This work is licensed under a Creative Commons Attribution 4.0 International License.
Read Full License

Additional Declarations: No competing interests reported.

Aluminum-modified silica achieves efficient removal of low fluoride wastewater by inducing crystallization

Shida Zhang [ab], Zhen Qi [ab], Fengke Dou [c], Weijie Zhong [c], Yingqiang Li [ab], Zheyu Wang [ab], Cui Zhen Sun, Feiyong Chen [a], Xue Shen [a]*, Rupeng Liu [a]*

[a] Institute of Resources and Environment Innovation, Shandong Jianzhu University, Jinan 250101, P.R. China

[b] School of Municipal and Environmental Engineering, Shandong Jianzhu University, Jinan 250101, P.R. China

[c] Shandong Coal Field Geological Survey and Research Institute, Jinan 250101, P.R. China

** Corresponding author:*

Xue Shen, E-mail: shenxue20@sdjzu.edu.cn; Tel: +86-17862922336;

Rupeng Liu, E-mail: liurupeng@sdjzu.edu.cn; Tel: +86-13305310386.

Abstract

The fluoride content in water environments has gradually increased with industrial development, and the existing technologies have limitations in treating low-fluoride wastewater. This study developed a novel aluminum-modified silica seed material (Al@SiO_2) via co-precipitation for fluoride removal through induced crystallization. The synergistic removal mechanism was systematically investigated. Characterization revealed that the Al@SiO_2 seed possessed a large pore diameter and surface aluminum hydrolysis products, which provided abundant sites for crystal growth. Hadrochemical simulation indicated that fluorapatite ($Ca_5(PO_4)_3F$) formation is most favorable at

neutral pH. However, the presence of bicarbonate ions (HCO_3^-) can inhibit fluoride removal by competing with phosphate (PO_4^{3-}) for calcium ions (forming $CaCO_3$) and consuming dihydrogen phosphate (e.g., $H_2PO_4^-$) species. Process parameters were optimized using response surface methodology. Under the optimal conditions—a Ca: P: F molar ratio of 10:5:1, a seed dosage of 2 mg/L, and a reaction time of 60 min—fluoride removal efficiency reached 85.47%, with the residual concentration stabilized below 1 mg/L. Characterization of the seeds before and after the reaction demonstrated that fluoride removal proceeds via two concurrent mechanisms: fluorapatite crystallization plays a major role, complemented by chemisorption through Al-F complexation. This work confirms that induced crystallization using $Al@SiO_2$ is an effective and promising strategy for treating low-fluoride wastewater.

Keywords: Seed crystal, Fluoride removal, Induced crystallization, Aluminum modification, Response surface method.

1. Introduction

Fluorine, a non-metallic chemical element, predominantly exists in nature as fluoride compounds (R. Wang et al. 2025). Its unique physicochemical properties render it an element of significant research value within the environmental geochemical cycle (B. He et al. 2023). With the advancement of industries such as metal smelting, battery manufacturing, and cement production, the discharge of fluorine-containing wastewater has increased correspondingly (Alhassan et al. 2022; Huang et al. 2020). The fluoride ion (F^-) concentration in such industrial effluents can reach 2000 mg/L or higher (Ayoob

et al. 2008). Excessive fluorine intake adversely affects human thyroid function and cognitive capacity; moreover, studies indicate it may lead to fluorosis, causing specific pathological changes in teeth, bones, and surrounding tissues (Chen et al. 2025; Xia et al. 2024). Consequently, the removal of fluoride from environmental media is critically urgent.

Various techniques have been employed for fluoride removal, including adsorption, chemical precipitation, electrochemical methods, membrane separation, and induced crystallization (Meena et al. 2024; Jiang et al. 2025; Vasylyeva et al. 2026). For high-concentration fluoride wastewater, combined processes are often necessary. However, these methods present inherent limitations: adsorption capacity is finite, chemical precipitation frequently generates substantial sludge, electrochemical systems are sensitive to water quality variations, and membrane technologies suffer from high energy consumption and module costs (Aoudj et al. 2012; Bai et al. 2019; Lim et al. 2021; C. He et al. 2022).

The induced crystallization method for fluoride removal represents an advancement over conventional precipitation. This technique involves introducing a crystalline carrier (seed crystal) into fluoride-containing wastewater prior to adding a precipitating agent. Upon reaching a supersaturated state, F^- and the precipitant undergo a crystallization reaction on the seed surface, forming new crystals that promote particle growth, thereby achieving fluoride removal (Agrawal et al. 2018). This approach offers high treatment efficiency, low operating cost, broad applicability, and minimized

secondary pollution (Zou and Wang 2016). Research on induced crystallization has predominantly focused on high-concentration systems (F^- > 100 mg/L), where the elevated initial concentration more readily achieves the supersaturation required for effective calcium fluoride (CaF_2) crystallization (Li et al. 2025). In contrast, for low-concentration fluoride wastewater (F^- < 10 mg/L), the extremely low degree of supersaturation hinders effective nucleation, resulting in poor treatment efficacy. While excessive calcium salts addition can improve sedimentation, it leads to sharply increased water salinity and excessive impurity ions, presenting major bottlenecks for the technology's application (R. Hu et al. 2024). Commonly used quartz sand seed crystals in current induced crystallization processes can reduce F^- levels in industrial wastewater to approximately 10 mg/L, yet struggle to meet the stringent discharge limit of 1.0 mg/L (Biswas et al. 2018). Therefore, modifying silica-based seed crystals to enhance fluoride removal performance holds substantial industrial application potential.

Aluminum salts are widely utilized in adsorption and material modification for fluoride removal due to their low cost and their hydrolysis product, aluminum hydroxide colloid, which captures F^- through adsorption, ligand exchange, and co-precipitation (Alhassan et al. 2022). Numerous studies confirm that Al - OH groups on adsorbent surfaces serve as primary active sites, capable of forming hydrogen bonds and effectively binding fluoride ions (Q. Wang et al. 2020). For instance, aluminum-modified activated carbon has demonstrated enhanced adaptability to coexisting ions and a broader effective pH range (Miao et al. 2025). Furthermore, research shows that

loading ternary metal oxides in amorphous form onto biochar creates hydroxyl-active adsorption sites and positive charges, synergistically improving fluoride removal (M. Wang et al. 2026). These findings indicate that adsorbents incorporating aluminum exhibit promising potential for aqueous fluoride removal.

The objective of this study is to develop an efficient aluminum-modified silica seed crystal via a co-precipitation method. By shifting the target crystallization product from CaF_2 to the less soluble calcium fluorophosphate (e.g., $Ca_5(PO_4)_3F$), the efficiency of the induced crystallization process in treating low-concentration fluoride wastewater can be enhanced (Yang et al. 2025). This work systematically investigates the effects of key variables, including contact time, seed crystal dosage, precipitant ratio, mixing intensity, and coexisting ions-on the fluoride removal performance of the modified seeds. A multi-factor interaction model was constructed using response surface methodology to analyze the contribution of each variable to the removal rate and their synergistic mechanisms, thereby establishing optimized operational parameters. Furthermore, the seed crystals were characterized before and after reaction using various techniques to elucidate the induced crystallization mechanism and explore the underlying fluoride removal pathways. By precisely regulating the phosphate-to-calcium ions ratio, this study achieves efficient and deep removal of low-concentration fluoride, providing technical support for the practical application of the induced crystallization method.

2. Materials and methods

2.1 Materials

Chemical reagents of analytical grade include HCl, NaOH, $NaNO_2$, $NaNO_3$, Na_2SO_4, Na_2CO_3, $NaHCO_3$, Na_2HPO_4, $AlCl_3 \cdot 6H_2O$, tetraethyl orthosilicate, Ammonium hydroxide, and anhydrous ethanol. Dissolve 2.21 g of dry sodium fluoride in 1 L volumetric flask to prepare 1 g/L fluoride reserve solution. In the experiment to study the influence of coexisting ions, a stock solution of coexisting anions with a concentration of 400 mg/L is prepared by precisely weighing $NaNO_2$, $NaNO_3$, Na_2SO_4, Na_2CO_3, $NaHCO_3$, Na_2HPO_4, and adding them respectively to 250 ml volumetric flutes. The pH value of the solution is adjusted with 0.1 mol/L HCl and NaOH. All the reagents mentioned above were of analytical pure grade, and Milli-Q water was utilized for the experiments.

2.2 Preparation of modified crystal seeds

2.2.1 Preparation of SiO_2

In a 250 mL beaker, add 50 mL of ultrapure water and 100 mL of anhydrous ethanol as solvents, and stir at 400 rpm for 5 min. Then, add 4 mL of ethyl n-silicon acetate (TEOS) to the beaker and stir for 5 min to mix evenly. Finally, add 6 mL of concentrated ammonia water. Stir at 600 rpm for 60 min. After the end of the stirring time, the mixture is allowed to stand for a period of time for centrifugal and then washed three times with ultrapure water and absolute ethanol, respectively, and dried in an oven at 70 ℃.

2.2.2 Preparation of Al@SiO_2

The modified seed $Al@SiO_2$ is obtained by loading aluminum onto silica by the co-precipitation method. The specific steps are as follows. Put $AlCl_3 \cdot 6H_2O$ into a beaker and stir for 15 min to ensure it is fully dissolved and evenly distributed. Then add an appropriate amount of TEOS and stir at 400 rpm for 15 min to mix it evenly with the solution. After the stirring is completed, add concentrated ammonia water drop by drop. Adjust the speed to 600 rpm and stir for 60 min. Then let it stand. After a period of time, perform centrifugal separation. Wash twice with ultrapure water and anhydrous ethanol, respectively, and then dry in a 70 ℃ oven for later use. The preparation schematic diagram is shown in Fig. S1.

2.3 Fluoride removal experiments

First, measure 150 mL of raw water and put it on the First, measure 150 mL of raw water and put it on the six-joint stirrer. Add a certain amount of crystal seeds to the raw water, stir for 5 min at a speed of 200 rpm to ensure thorough mixing of the crystal seeds with the solution. Then, add a certain amount of phosphate solution, keep the speed constant, and stir for 5 min to ensure uniform mixing of the phosphate with the solution. Then add a certain amount of calcium salt solution, keep the rotational speed constant, stir for 5 min to ensure the calcium salt is evenly mixed with the solution, and continue to stir for 60 min. Set the rotational speed of the stirrer to 100 rpm. After the process is completed, conduct the measurement. Add a certain amount of crystal seeds to the raw water, stir for 5 min at a speed of 200 rpm to ensure thorough mixing of the crystal seeds with the solution. Then, add a certain amount of phosphate solution, keep

149 the speed constant, and stir for 5 min to ensure uniform mixing of the phosphate with
150 the solution. Then add a certain amount of calcium salt solution, keep the rotational
151 speed constant, stir for 5 min to ensure the calcium salt is evenly mixed with the solution,
152 and continue to stir for 60 min. Set the rotational speed of the stirrer to 100 rpm. After
153 the process is completed, conduct the measurement. The removal of F^- is measured by
154 using the FE20K PLUS multi-parameter analyzer.

155 2.4 Characterization

156 The surface morphology of different crystal seeds was observed by scanning electron
157 microscopy (SEM; Zeiss Merlin Compact, Zeiss, Germany). Surface chemical
158 composition analysis was detected by the energy dispersive X-ray spectroscopy (EDS;
159 Bruker 6/30, Zeiss, Germany). The phase identification of the modified crystal seeds
160 was carried out by X-ray diffraction (XRD, D8 Advance, Bruker, Germany) The
161 specific surface area and pore volume of difference crystal seeds were characterized
162 using a Specific Surface Area and Pore Volume Analyzer (BET, autosorbiQ, Quanta
163 chrome, USA). The X-ray photoelectron spectroscopy (XPS, K-Alpha, Thermo, USA)
164 was utilized to analyze the elemental composition and valence state changes on the
165 surface of the seed crystal.

166 ## 3. Results and discussion

167 3.1 Characterization of modified crystalline particles

168 3.1.1 Analysis of morphology and elemental composition

169 Fig. 1 presents the SEM images of different crystal seeds. The surface of the raw

quartz sand seeds is smooth and flat, with no distinct edges or visible porosity, exhibiting a certain gloss (Fig. 1A-C). In contrast, the synthesized SiO_2 particles (Fig. 1D-E) display a uniform spherical morphology but lack obvious pores on their surface. After aluminum modification, the Al@SiO_2 seeds (Fig. 1F-H) show a distinctly altered surface, covered with coarse deposits and exhibiting a clearly developed porous structure. This indicates that the modification process increased the seed's porosity and expanded its specific surface area, thereby providing more attachment sites for fluoride crystal precipitation and significantly enhancing F^- removal efficiency. EDS analysis (Fig. S2) reveals that the silicon content in the synthesized SiO_2 slightly increased compared to the raw quartz sand. Furthermore, the primary components of Al@SiO_2 are Si, O and Al, with elemental mass percentages of 30.25 wt%, 44.56 wt% and 22.06 wt%, respectively. The decrease in the detected Si signal can be attributed to the coverage of the seed surface by Al-containing compounds formed during modification.

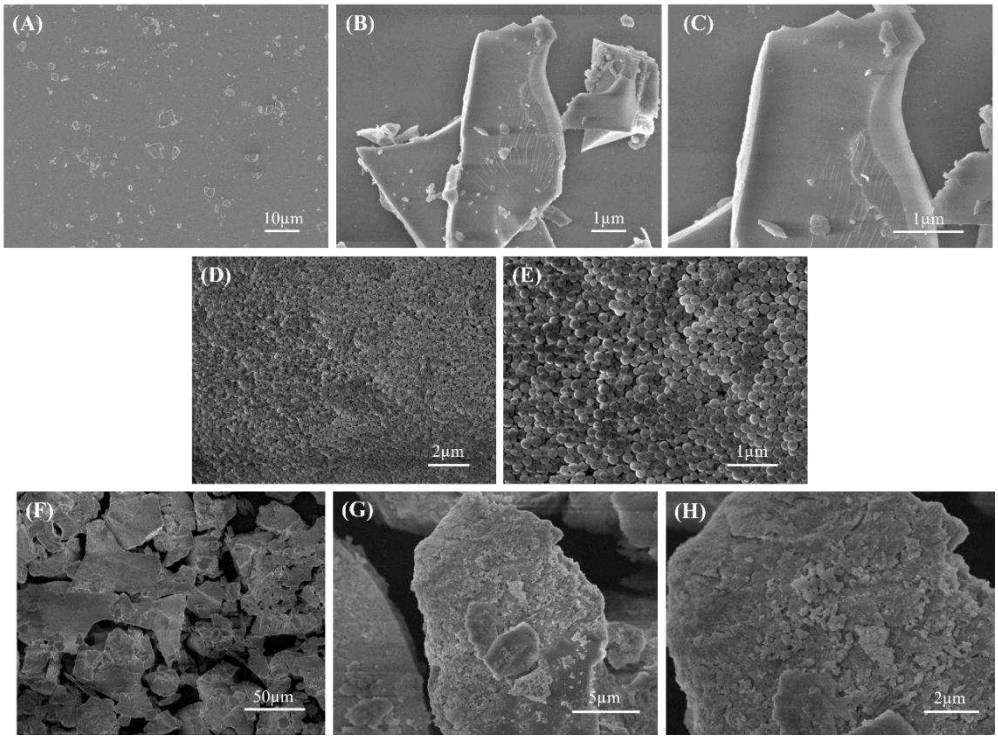


Fig. 1. SEM images of quartz sand magnified 1000, 10000 and 20000 times (A-C), SiO_2 magnified 8000, 20000 times (D-E), and Al@SiO_2 magnified 500, 5000, 10000 times (F-H) respectively.

3.1.2 XRD and BET analysis

The phase composition of the Al@SiO_2 seed was determined by XRD, as shown in Fig. 2. The XRD pattern displays characteristic diffraction peaks at approximately 20.96°, 26.64°, 36.54°, and 39.60°, which align with PDF#77-1060 (SiO_2). In the meantime, the peaks at approximately 18.28°, 20.28°, 26.88°, and 37.66°, which align with PDF#74-17750, indicates the presence of $Al(OH)_3$ in the modified seed (Lv et al. 2023). This confirms the successfully loading of aluminum onto SiO_2 and the formation of Al hydroxide. The resulting aluminum hydroxide colloid can capture F^- through adsorption, ligand exchange, and co-precipitation, thereby improving removal efficiency.

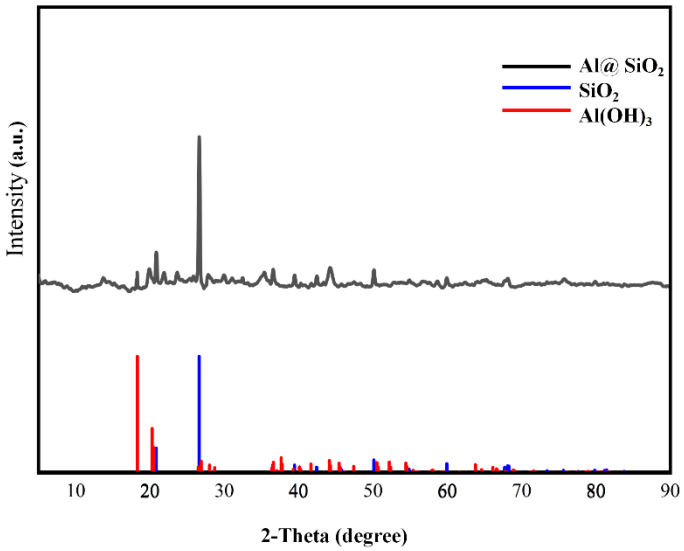


Fig. 2. XRD patterns of the Al@SiO_2.

Specific surface area, pore volume and pore size are crucial parameters influencing the crystallization performance of seed materials. The N_2 adsorption-desorption isotherms of quartz sand, SiO_2, and Al@SiO_2 are compared (Fig. 3A-C). Both quartz sand and SiO_2 exhibit nearly coincident adsorption and desorption curves without a hysteresis loop. In contrast, the isotherm for Al@SiO_2 is of type IV (IUPAC), with a distinct hysteresis loop, indicating the presence of a mesoporous structure. The lack of a clear saturation plateau suggests an irregular pore size distribution, consistent with SEM observations (Fig. 2F-H). The pore size distribution (Fig. 3D) further confirms that quartz sand and SiO_2 possess negligible porosity, while Al@SiO_2 is predominantly mesoporous (2–50 nm), with most pores between 5–30 nm, a structure conducive to enhanced adsorption.

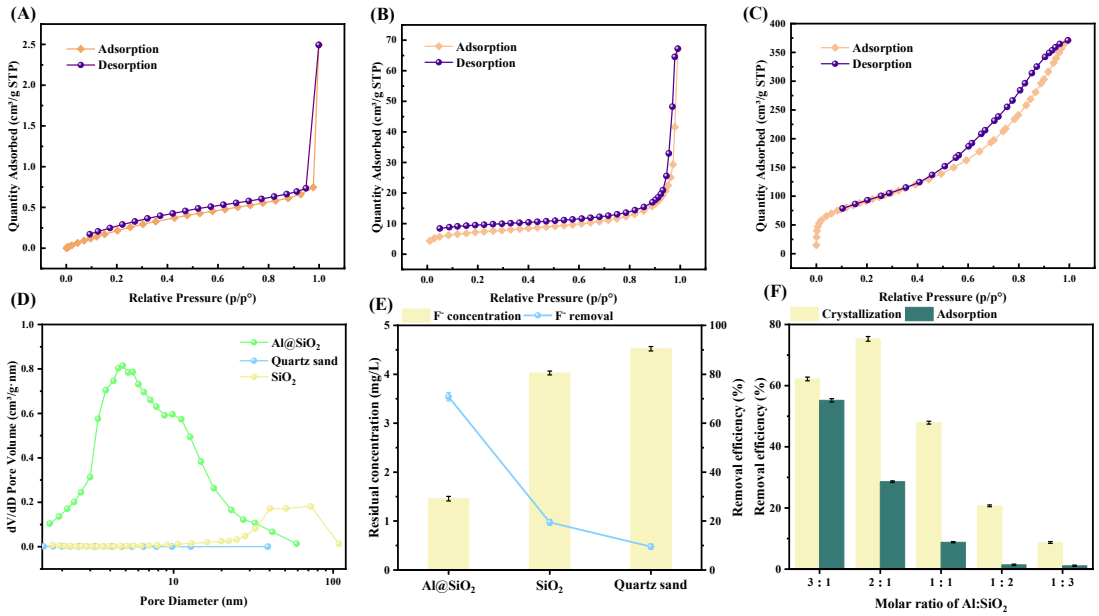


Fig. 3. The adsorption and desorption curves of (A) quartz sand, (B) SiO_2 and (C) $Al@SiO_2$, (D) the pore size distribution of different seed crystal. (E) The fluoride removal effects of different crystal species and (F) the removal effect of fluoride by adsorption and induced crystallization under different molar ratios of aluminum to silicon.

The specific surface area parameters are summarized in Table S1. The BET specific surface areas of quartz sand, SiO_2 and $Al@SiO_2$ are 1.3278 m^2/g, 23.8486 m^2/g and 334.6332 m^2/g, respectively. The corresponding total pore volumes are 0.003858 cm^3/g, 0.034372 cm^3/g and 0.571080 cm^3/g, and the average pore diameters are 11.6210 nm, 5.7651 nm and 6.8263 nm, respectively. Notably, the specific surface area and total pore volume of $Al@SiO_2$ are approximately 330 and 14 times greater than those of quartz sand and SiO_2, respectively. The slight reduction in the average pore diameter of $Al@SiO_2$ compared to quartz sand can be attributed to the loading and accumulation of aluminum species on the material surface, partially blocking some original pores.

225 Nevertheless, the substantially larger specific surface area and pore volume of Al@SiO_2
226 increase the probability of contact with F^- and provide more sites for crystalline product
227 attachment.

228 The fluoride removal performance of the different seeds is compared in Fig. 3E. The
229 modified seed Al@SiO_2 achieves the highest F^- removal efficiency (70.84%), which is
230 approximately 7.4 times that of quartz sand (9.54%). The synthesized SiO_2 shows an
231 intermediate removal efficiency of 19.45%, about twice that of quartz sand. Fig. 3F
232 illustrates the effect of the Al: SiO_2 molar ratio on F^- removal via combined
233 crystallization and adsorption. The results indicate that removal efficiency is
234 significantly higher when Al: $SiO_2 > 1$ compared to ratios $\leqslant$ 1. Specifically, the
235 efficiency at a 2:1 ratio was 9 times higher than that at a 1:3 ratio, demonstrating that
236 higher aluminum content enhances performance, with an optimum at Al: SiO_2 = 2:1.
237 However, beyond this optimum, further increasing the aluminum content shifted the
238 dominant mechanism from crystallization to adsorption. This shift is consistent with
239 the BET analysis, which suggested that excessive Al loading might compromise the
240 porous structure favorable for crystallization. Moreover, seeds with high Al content
241 competitively adsorb not only F^- but also phosphate (PO_4^{3-}) and calcium (Ca^{2+}) ions.
242 This reduces the ionic supersaturation in solution, hindering crystallization and
243 ultimately compromising overall F^- removal. characterization and performance data
244 confirm that Al@SiO_2 removes F^- through a combined mechanism of adsorption and
245 crystallization, with its efficiency highly dependent on the optimized Al content and

246 textural properties.

247 3.1.3 The effect of seed dosage

248 This section examines the effects of key parameters, including seed dosage, reagent
249 dosage, reaction time, rotational speed, and initial pH on fluoride removal by $Al@SiO_2$.
250 The corresponding results are presented in Fig. 4. The F^- removal efficiency of
251 $Al@SiO_2$ significantly surpassed that of raw quartz sand across all tested dosages (Fig.
252 4A). For quartz sand, increasing the dosage did not markedly improve performance,
253 while the F^- removal rate of $Al@SiO_2$ gradually increases and the remaining F^-
254 concentration continuously decreases. This could be explained to that with the dosage
255 increases, the contact probability increases and $Al@SiO_2$ has a larger specific surface
256 area, providing more active sites for the nucleation and growth (or deposition) of
257 fluoride-containing crystals.

258 When the dosage exceeded 2 g/L, the residual F^- concentration stabilized below 1
259 mg/L. However, the rate of efficiency improvement diminished beyond this point. This
260 phenomenon could be explained by that the concentration of crystal seeds keeps
261 increasing, leading to a higher probability of collision between seed particles, which
262 may disrupt the crystal growth process, and reduce the overall crystallization efficiency.
263 At the same time, the increase in dosage will also increase the reaction cost. Therefore,
264 the dosage for subsequent experiments is set at 2 g/L.

265 3.1.4 The effect of the molar ratios of P: F

266 As shown in Fig. 6B, $Al@SiO_2$ achieved superior F^- removal compared to SiO_2

267 across various P: F molar ratios. As the P:F ratio increased from 0 to 5, the concentration
268 of PO_4^{3-} in solution rose, and the F^- removal efficiency increased correspondingly from
269 38.65% to approximately 85%. Beyond a ratio of 5, further addition of PO_4^{3-} produced
270 no significant improvement in F^- removal, with the residual concentration stabilizing
271 below 1 mg/L. This indicates that the combined contamination of PO_4^{3-} and F^- can be
272 effectively treated, while also reducing overall chemical consumption (R. Hu et al.
273 2025). However, excessive phosphate concentrations could promote the release of
274 fluoride from crystalline products (Christoffersen et al. 1988). Therefore, considering
275 both process economics and the risk of fluoride re-release, a P: F molar ratio of 5 was
276 selected for all subsequent experiments.

277 3.1.5 The effect of the molar ratios of Ca: F

278 As shown in Fig. 4C, the F^- removal effect of Al@SiO_2 is superior to that of SiO_2
279 under different molar ratios of Ca: F. As the dosage of the calcium source increased
280 (raising the Ca^{2+} concentration), the F^- removal efficiency rose from 25.25% to 84.72%,
281 while the residual F^- concentration dropped from 3.73 mg/L to below 1 mg/L. The
282 optimal ratio was observed at Ca: F = 10:1. Beyond this point, further addition of
283 calcium yielded no significant improvement in removal, indicating a plateau in
284 performance. Therefore, considering removal efficiency and reagent economy, a Ca: F
285 molar ratio of 10:1 was selected for all subsequent experiments.

286 3.1.6 The effect of stirring speed

287 The effect of stirring speed on fluoride removal via Al@SiO_2-induced crystallization

288 is shown in Fig. 4D. The results indicate that the F^- removal efficiency improved with
289 increasing stirring speed. This enhancement is attributed to better dispersion of the seed
290 material. At higher speeds, seed crystals that would otherwise settle at the bottom
291 become uniformly suspended in the solution. This increases the contact probability
292 between the seeds and F^-, providing more sites for crystal attachment and growth,
293 thereby improving the overall removal performance.

294 3.1.7 The effect of stirring time

295 The effect of reaction time on fluoride removal is shown in Fig. 4E. The residual F^-
296 concentration decreased progressively over time. At 15 min (the rapid mixing stage),
297 the removal efficiency is 47.73%, leaving 2.44 mg/L F^- in solution. The efficiency
298 increased to 51.26% shortly thereafter. With further extension of the reaction time, the
299 residual F^- decreased to 0.92 mg/L at 40 min and to 0.75 mg/L at 60 min. Beyond 60
300 min, with the reaction time continued to increase, there is an insignificant improvement
301 in the F^- removal effect. Therefore, the reaction time for subsequent experiments was
302 set to 60 min.

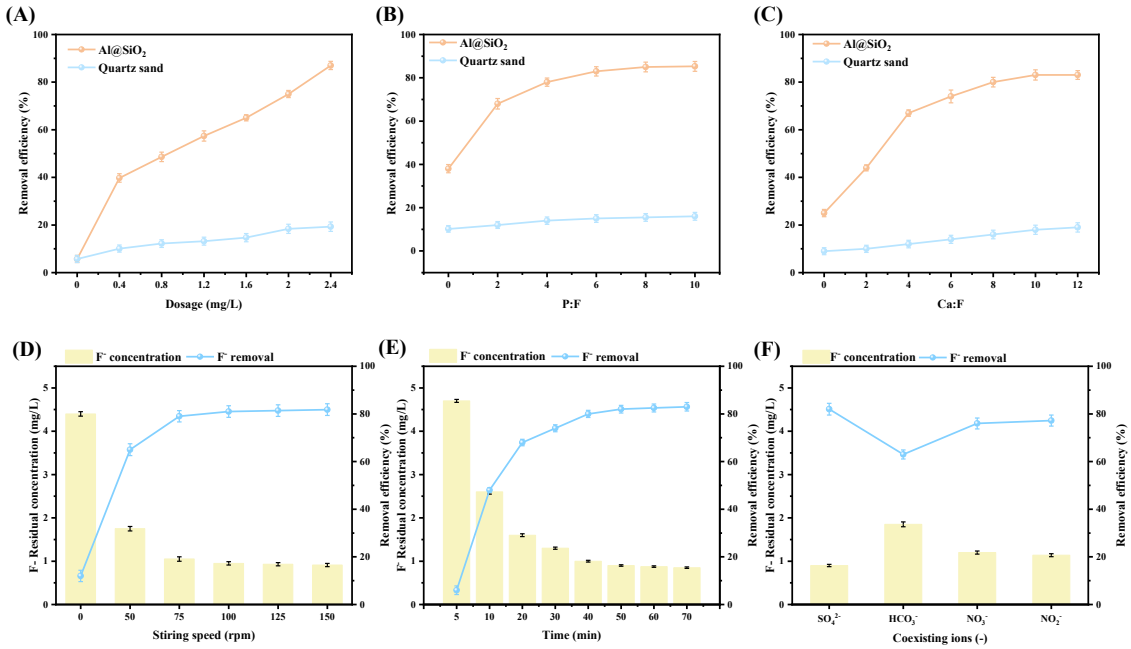


Fig. 4. The influence of different factors including (A) dosage, (B) the molar ratio of P: F, (C) the molar ratio of Ca: F, (D) stirring speed, (E) stirring time, and (F) diverse coexisting ions on the removal effect of fluoride.

3.1.8 The effect of co-exist ions

Studies proclaim that the presence of certain ions may affect the removal of target pollutants. Thus, this experiment simulates the effect of adding common pollutants on the removal of F^-. The simulated concentration is 1 mmol/L, and the pollutants include SO_4^{2-}, HCO_3^-, NO_3^- and NO_2^- in Fig. 4F. Results show that SO_4^{2-}, NO_3^-, and NO_2^- have no significant impact on the F^- removal effect, but CO_3^{2-} shows a greater influence on the F^- removal effect, reducing the removal rate to 63.2%. This effect may be attributed to the competitive Ca^{2+} binding between HCO_3^- and F^-, and the CO_3^{2-} ionised from HCO_3^- combines with Ca^{2+} to form $CaCO_3$ precipitate (Fu et al. 2025). This leads to the remaining PO_4^{3-} in the solution, and the HCO_3^- will also react with the $H_2PO_4^-$, reducing

317 the F^- removal.

318 The efficiency of fluoride removal via crystallization as $Ca_5(PO_4)_3F$ is strongly pH-
319 dependent, as pH governs the solubility of the mineral and the speciation of key ions
320 (Feng et al. 2025). Fig. 5A shows the removal performance across different initial pH
321 values. The residual F^- concentration was highest (2.34 mg/L) at pH 4, remained around
322 or below 1 mg/L in the near-neutral range (pH 6-8), and increased again under alkaline
323 conditions. Speciation modelling using Visual MINTEQ 3.1 (Fig. 5B-E) explains these
324 trends. In acidic media (pH ~4), a significant fraction of fluoride exists as HF, and
325 phosphate is primarily present as $H_2PO_4^-$, both of which are less reactive in the
326 crystallization process. The concentration of reactive $Al(OH)_3$ is also low. These factors
327 collectively reduce the efficient crystallization, lowering F^- removal. In the optimal pH
328 range of 6-8, aluminum exists predominantly as $Al(OH)_3$, which provides effective
329 adsorption sites, while calcium remains as free Ca^{2+} ions. The buffering capacity
330 provided by the phosphate source (NaH_2PO_4) helps maintain this favorable condition,
331 resulting in stable and high removal efficiency. Under highly alkaline conditions (pH
332 10), the buffering capacity is exceeded. The formation of $CaOH^+$ species reduces the
333 concentration of free Ca^{2+}, limiting precipitate formation and leading to poor F^- removal.
334 Therefore, an initial pH between 6 and 7 was selected for all subsequent experiments
335 to ensure optimal and stable performance.

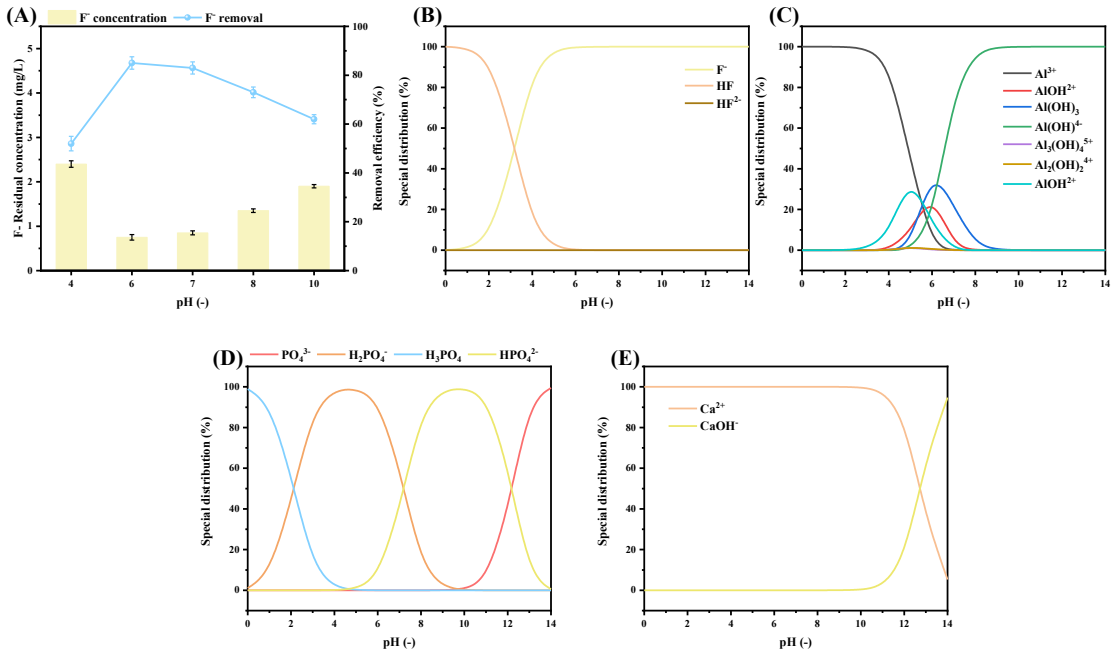


Fig. 5. The influence of pH on the fluoride removal (A), water chemistry simulation diagrams of ionic forms of different ions changing with pH.

3.2 Response surface analysis of F^- removal and model validation

3.2.1 Model validation

The Box-Behnken design (BBD) was employed to investigate the influencing factors and their interactions. Four variables - seed dosage (A), P: F molar ratio (B), Ca: F molar ratio (C), and reaction time (D) were selected based on single-factor experiments (Table S1). Within the appropriate ranges determined from single-factor tests, three levels for each factor were set to design a four-factor, three-level experiment matrix. A total of 28 experiments were performed according to this design (Table S2). The relationship between the response variable (removal efficiency, %) and the four independent variables was modeled using a second-order polynomial equation (Eq. 1).

$$Y = -193.77594 + 158.32500 * A + 9.85271 * B + 11.56333 * C + 0.808063 * D - 0.868750 * AB - 2.06875 * AC + 0.014688 * AD - 0.238750 * BC + 0.024438 * BD + 0.009188 * CD - 31.66927 * A^2 - 0.665521 * B^2 - 0.294896 * C^2 - 0.008268 * D^2 \quad (1)$$

Analysis of Variance (ANOVA) was used to assess the model's adequacy. The detailed ANOVA results are presented in Table S3. The model's F- value of 70.06 and a p- value<0.0001 indicate that the regression is highly significant. It showed an excellent fit, with a coefficient of determination (R^2) of 0.9869. The model's reliability was confirmed by the close agreement between the adjusted R^2 (0.9736) and the predicted R^2 (0.9595), with a difference of only 0.0141 (< 0.2). The low coefficient of variation (CV = 0.78%) demonstrated good experimental precision and reproducibility. All four quadratic terms (A, B, C, D) had p-values < 0.01, indicating their significant influence on F^- removal. Based on the magnitude of their effects in the model, the order of significance for the factors was: seed dosage (A) > Ca: F molar ratio (C) > reaction time (D) > P: F molar ratio (B).

The diagnostic plots confirm the model's validity. The residuals closely follow a normal distribution, as evidenced by their alignment along the reference line in the normal probability plot (Fig. 6A) (Meena et al. 2024). Furthermore, the strong agreement between predicted and actual values in Fig. 6B, with experimental points evenly scattered around the ideal fit line, further confirms the model's reliability for predicting fluoride removal efficiency (Nazari et al. 2014).

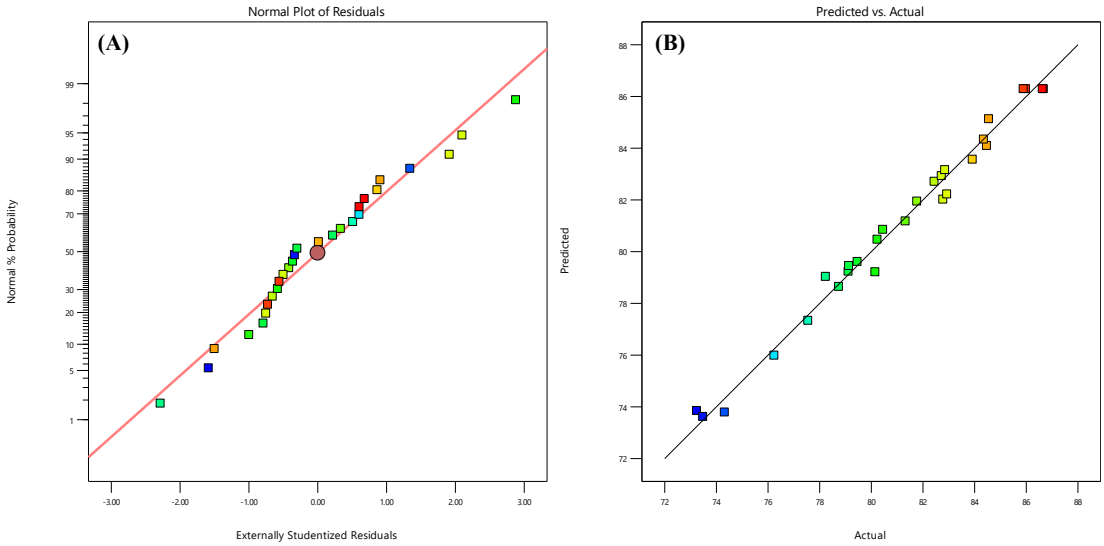


Fig. 6. (A) Standard residual analysis diagram and the relationship graph between the (B) predicted value and the actual value.

3.2.2 Response surface analysis

The 3D response surface plots illustrate the interactions among the four factors: (A) seed dosage, (B) P: F molar ratio, (C) Ca: F molar ratio, and (D) reaction time (Fig. 7). Both the contour shapes and surface curvatures indicate that all four factors exerted significant individual positive effects on fluoride removal efficiency within the tested ranges. The interaction between factor A and factor B was particularly significant, as evidenced by the elliptical contour plot and dense contours in Fig. 7A. The response surface shows that removal efficiency increases to an optimum before declining at higher levels of both factors. This decline is consistent with the known inhibitory effect of excessive phosphate on calcium fluoride crystallization and its potential to promote fluoride release from crystal products. Similarly, the interactions between A and C (Fig. 7B), B and C (Fig. 7D), and B and D (Fig. 7E) were also significant, indicated by their elliptical contours and high contour density. In contrast, the interactions for AD (Fig.

7C) and CD (Fig. 7F) were not significant, as shown by their near-circular contours with low density. This visual interpretation aligns well with the statistical conclusions from the ANOVA.

The process parameters were optimized to maximize F^- removal efficiency. The model predicted optimum conditions were: seed dosage = 2.08 g/L, P: F molar ratio = 5.43, Ca: F molar ratio = 10.51, and reaction time = 64.22 min, corresponding to a predicted removal efficiency of 86.57%.To validate the model, three verification experiments were conducted using practical approximations of these conditions (2.1 g/L, P: F = 5.4, Ca: F = 10.5, 64 min). The average experimental removal efficiency was 85.58%, with the residual F^- concentration stably below 1 mg/L. The relative error between the experimental and predicted values was only 1.16%, demonstrating excellent agreement and confirming the model's high predictive accuracy.

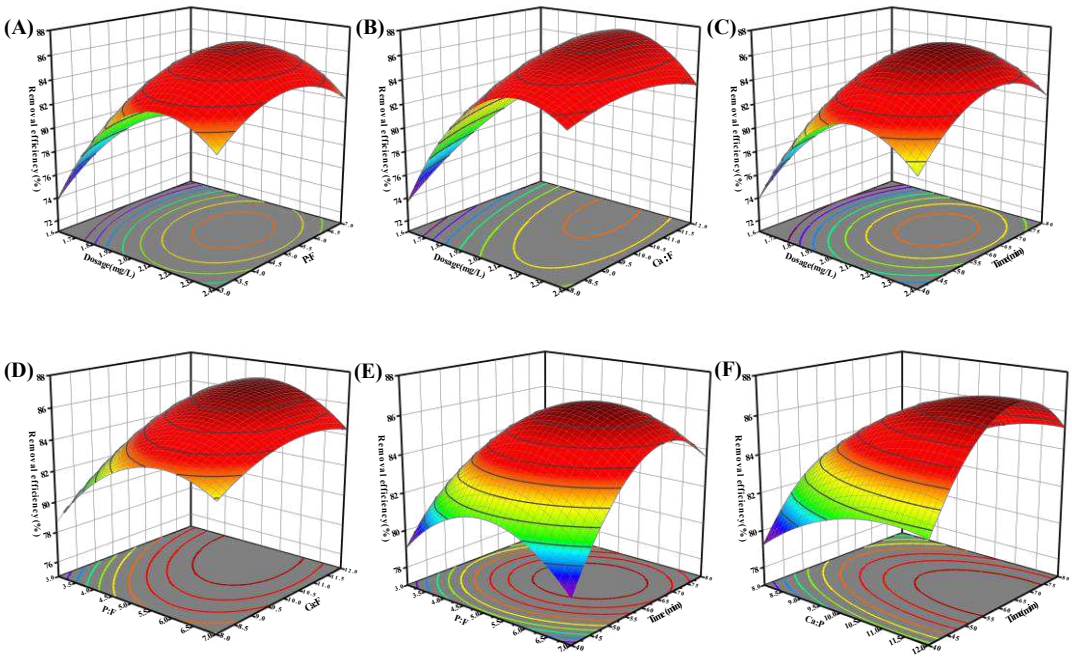


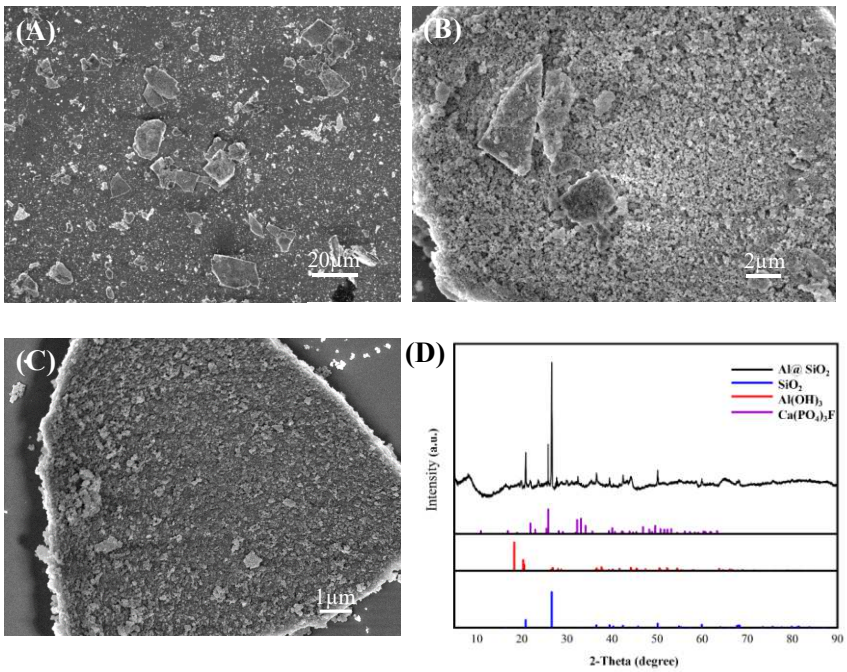
Fig. 7. 3D surface plots for fluoride removal illustrate the interaction effect of the

seed dosage, P: F, Ca: F, and reaction time.

3.3 Analysis of removal mechanism

SEM images reveal distinct changes in the morphology of the Al@SiO_2 seeds before and after the fluoride removal reaction Fig. 1(F-H) & Fig. 8. Before the reaction, the seed surface was rough but with only sparse, dispersed particles, leaving substantial areas exposed. After the reaction, the surface became significantly rougher and was fully covered by a dense, closely packed layer of material, with no exposed areas visible. This complete surface coverage indicates the growth and attachment of crystalline products onto the seed. EDS analysis confirmed the composition change (Fig. S2-S3). The unreacted seeds contained primarily O, Si, and Al. After the reaction, new peaks for Ca, P, and F appeared (the C signal originates from the conductive adhesive used in sample preparation). The presence of Ca, P, and F together indicates the successful formation and attachment of $Ca_5(PO_4)_3F$ on the seed surface. The increased surface area and coverage provided by this crystalline layer likely contribute to the enhanced fluoride removal efficiency observed during the reaction.

The phase composition of the reacted Al@SiO_2 seeds was analyzed by XRD (Fig. 8D). The pattern confirmed the presence of SiO_2 (peaks at 20.96°, 26.64°, 36.54°, and 39.60° 2θ) and $Al(OH)_3$ (with diffraction peaks at 18.28°, 20.28°, 26.88°, and 37.66° at 2θ). Additionally, new peaks at approximately 25.86°, 31.92°, 33.10°, and 46.88° 2θ were observed, matching the standard pattern for fluorapatite, $Ca_5(PO_4)_3F$ (PDF#15-0876). This proved that there is $Ca_5(PO_4)_3F$ exists in the crystal seed surface.



418

419 Fig. 8. The SEM image of Al@SiO_2 crystal seeds after the reaction magnified (A)

420 500, (B) 5000, (C) 10000 times and (D) XRD patterns of the Al@SiO_2.

421 XPS was employed to analyze the surface chemical states of the Al@SiO_2 seed after

422 the fluoride removal reaction, with the results presented in Fig. 9. The characteristic

423 peaks of C, O, Si, Al, Ca, F, and P were detected on the full spectrum of the XPS scan

424 after the reaction in Fig. 9A compared to the full spectrum of the XPS scan before the

425 reaction (Fig. S4). The appearance of Ca, P, and F signals, consistent with the EDS

426 results (Fig. S3), indicates that the $Ca_5(PO_4)_3F$ is formed on the surface of Al@SiO_2.

427 The detected carbon is attributed to common adventitious hydrocarbon contamination.

428 In the high-resolution C1s spectrum (Fig. 9B), three peaks at 284.8 eV, 286.4 eV, and

429 289.15 eV correspond to C-C/C-H, C-O, and O-C=O bonds, respectively (Liu et al.

430 2022). In the O1s spectrum (Fig. 9C), the peaks located in 531.6 eV and 532.8 eV could

431 be assigned to hydroxyl groups and adsorption water. In Fig. 9D, the peaks at 101.7 eV

(Aluminosilicate) and 102.6 eV (Si-F-O) suggest an interaction between Si and F^- during the adsorption process. For Al2p (Fig. 9E), the characteristic peaks at 73.61 eV and 74.43 eV could be regarded as the Al-O and Al-OH. Moreover, the peak at 75.15 eV (Al-F) confirms fluoride chemisorption via complex formation (H et al. 2024; W. Hu et al. 2025). The Ca2p spectrum (Fig. 9F) showed a doublet at 347.94 eV and 351.54 eV with a spin-orbit splitting of 3.6 eV, characteristic of calcium in a phosphate environment such as $Ca_5(PO_4)_3F$ (Zhang et al. 2025). Combined with the P2p and F1s spectra, the characteristic peaks in 685.34 eV, 133.60 eV, and 135.44 eV could prove that F^- are removed by forming calcium fluorophosphate(Fig. 9G-H) (Deng et al. 2021).

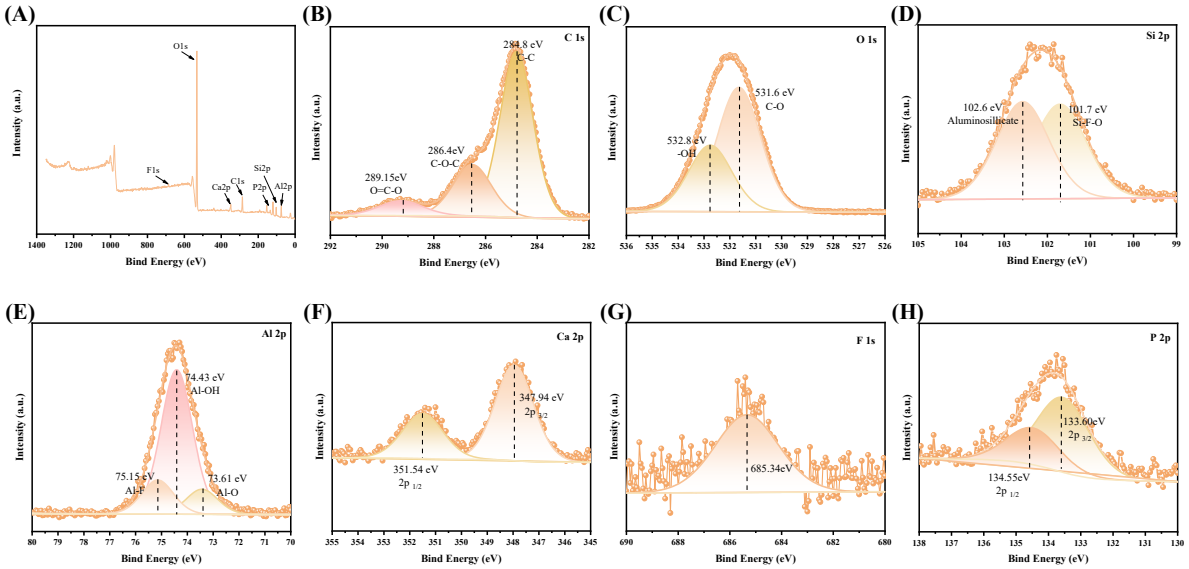


Fig. 9. XPS spectra of Al@SiO_2 after reaction: (A) the full spectrum, (B) C1s, (C) O1s, (D) Si2p, (E) Al2p, (F) Ca2p, (G) F1s and (H) P2p.

The combined evidence from XPS, XRD, and EDS conclusively demonstrates that fluoride removal by the Al@SiO_2 seed proceeds through two concurrent mechanisms. Specifically, fluorapatite crystallization serves as the primary pathway, which is

complemented by chemisorption via aluminum-fluoride complexation. This dual mechanism is further enhanced by the seed's modified structure: its developed porosity provides abundant nucleation sites, while the surface-bound aluminum (hydroxide) species offer effective adsorption sites for fluoride. To clarify this process, a schematic illustration of the dual removal mechanism is presented in Fig. 10.

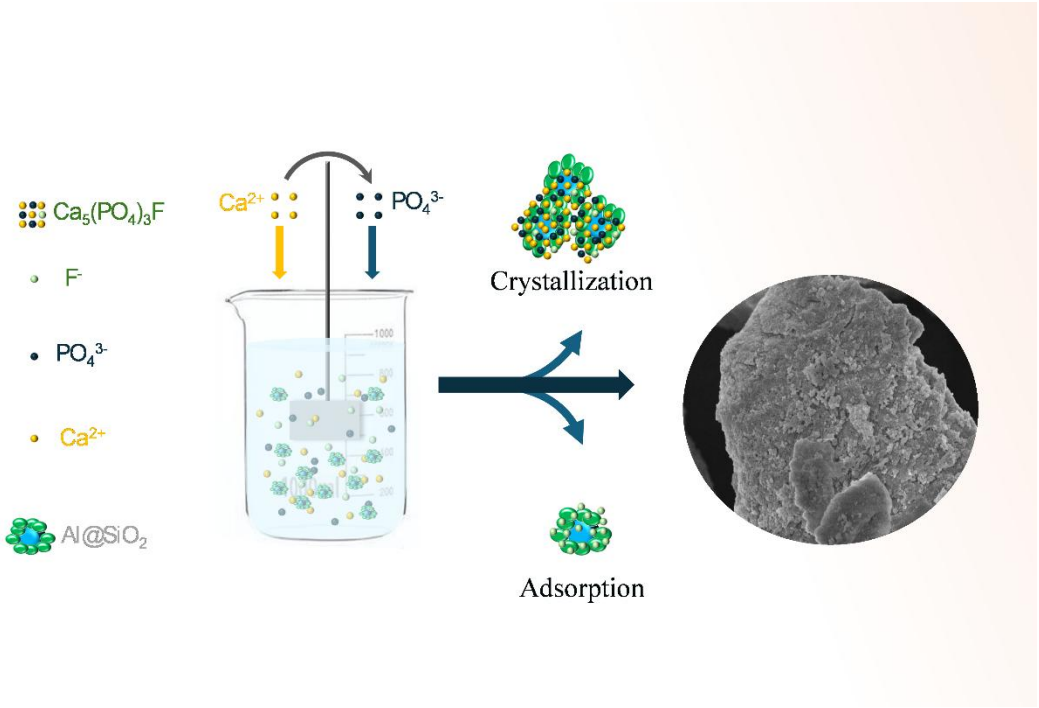


Fig. 13. Schematic diagram of fluoride removal mechanism.

4. Conclusion

In this study, aluminum-modified silica seed crystals were successfully synthesized via a co-precipitation method, significantly enhanced fluoride removal performance compared to unmodified quartz sand and pure SiO_2. The specific conclusions are as follows:

(1) The modification process substantially increased the specific surface area and pore volume of the seed material, providing abundant attachment sites for crystalline

products and thereby greatly improving the F^- removal efficiency.

(2) Single-factor experiments and response surface methodology were employed to investigate the effects and interactions of key operational parameters. The optimal conditions for F^- removal using Al@SiO_2 were determined as follows: seed dosage = 2.0 g/L, Ca: P: F molar ratio = 10:5:1, reaction time = 60 min, and stirring speed = 100 rpm. Under these conditions, the residual F^- concentration was stably reduced below 1.0 mg/L.

(3) Solution pH significantly influenced the removal process. Stable and efficient F^- removal was achieved within a pH 6-8. However, the presence of HCO_3^- markedly inhibited removal efficiency.

(4) Post-reaction characterization confirmed the formation of calcium fluorophosphate on the seed surface. The primary mechanism for F^- removal was identified as induced crystallization, with adsorption playing a synergistic role in the overall process.

This study demonstrates that aluminum-modified silica is a highly effective seed material for the induced crystallization removal of low-concentration fluoride, offering a promising approach for treating fluoride-contaminated wastewater.

CRediT authorship contribution statement

Shida Zhang: Methodology, Original draft preparation; Zhen Qi: Data curation; Fengke Dou: Validation; Weijie Zhong: Investigation; Yingqiang Li: Validation; Zheyu Wang; Reviewing; Cui Zhen Sun: Supervision; Feiyong Chen: Reviewing; Xue Shen: Investigation, Funding acquisition; Rupeng Liu: Funding acquisition.

Declaration of competing interest

The authors declare that they have no known competing financial interests or personal relationships that could have appeared to influence the work reported in this paper.

Acknowledgements

This work was funded by the Youth Innovation and Technology Plan of Universities in Shandong Province (2023KJ007); Basic Research Program of Jiangsu (BK20250159); National Natural Science Foundation of China (52270006); Doctoral Research Fund of Shandong Jianzhu University (No. X21076Z).

Data availability

Data will be made available on request.

Reference

Agrawal, S., Guest, J. S., & Cusick, R. D. (2018). Elucidating the impacts of initial supersaturation and seed crystal loading on struvite precipitation kinetics, fines production, and crystal growth. *Water Research*, *132*, 252–259. https://doi.org/10.1016/j.watres.2018.01.002

Alhassan, S. I., Wang, H., He, Y., Yan, L., Jiang, Y., Wu, B., et al. (2022). Fluoride remediation from on-site wastewater using optimized bauxite nanocomposite (bx-ce-la@500): synthesis maximization, and mechanism of F─ removal. *Journal of Hazardous Materials*, *430*, 128401. https://doi.org/10.1016/j.jhazmat.2022.128401

Aoudj, S., Drouiche, N., Hecini, M., Ouslimane, T., & Palaouane, B. (2012). Coagulation as a post-treatment method for the defluoridation of photovoltaic cell manufacturing wastewater. *Procedia Engineering*, *33*, 111–120. https://doi.org/10.1016/j.proeng.2012.01.1183

Ayoob, S., Gupta, A. K., Bhakat, P. B., & Bhat, V. T. (2008). Investigations on the kinetics and mechanisms of sorptive removal of fluoride from water using alumina cement granules. *Chemical Engineering Journal*, *140*(1), 6–14. https://doi.org/10.1016/j.cej.2007.08.029

Bai, Z., Hu, C., Liu, H., & Qu, J. (2019). Selective adsorption of fluoride from drinking water using NiAl-layered metal oxide film electrode. *Journal of Colloid and Interface Science*, *539*, 146–151. https://doi.org/10.1016/j.jcis.20

18.12.062

Biswas, G., Thakurta, S. G., Chakrabarty, J., Adhikari, K., & Dutta, S. (2018). Evaluation of fluoride bioremediation and production of biomolecules by living cyanobacteria under fluoride stress condition. *Ecotoxicology and Environmental Safety*, *148*, 26–36. https://doi.org/10.1016/j.ecoenv.2017.10.019

Chen, Q., Deng, J., & Luo, G. (2025). Highly selective removal of fluorine from wastewater containing phosphorus and fluorine in a microreaction system. *Separation and Purification Technology*, *358*, 130255. https://doi.org/10.1016/j.seppur.2024.130255

Christoffersen, Jør., Christoffersen, M. R., Kibalczyc, W., & Perdok, W. G. (1988). Kinetics of dissolution and growth of calcium fluoride and effects of phosphate. *Acta Odontologica Scandinavica*, *46*(6), 325–336. https://doi.org/10.3109/00016358809004784

Deng, L., Ou, J., Yang, H., Wen, G., & Huang, T. (2021). The surface regulation of calcite for defluoridation by fluorapatite-induced crystallization. *Journal of Water Process Engineering*, *41*, 102082. https://doi.org/10.1016/j.jwpe.2021.102082

Feng, B., Xue, Y., Wang, D., Chen, S., Zhang, S., Zhang, L., et al. (2025). Stability of lead immobilization by *aspergillus niger* and fluorapatite under different pH conditions. *Ecotoxicology and Environmental Safety*, *289*, 117706. https://doi.org/10.1016/j.ecoenv.2025.117706

Fu, Z., Wang, Y., Shi, X., Zhou, D., Li, Z., Jin, P., et al. (2025). Supersaturation mechanisms and regulation strategies in nucleation-induced crystallization f or high-purity fluoride recovery from photovoltaic wastewater. *Chemical E ngineering Journal*, *523*, 168353. https://doi.org/10.1016/j.cej.2025.168353

H, T., Chaabane, T., Omine, K., Sivasankar, V., Sano, H., Hecini, M., & Darchen, A. (2024). Simultaneous removal of fluoride and nitrate from an aqueous mixture and semiconductor wastewater by sodium chloride mediated electr o-generated aluminas (EGAs): conversion of recovered fluoride into fluora patite using plasterboard waste. *Journal of Cleaner Production*, *463*, 14273 0. https://doi.org/10.1016/j.jclepro.2024.142730

He, B., Zhu, Y., Zu, Y., Nie, Y., & Mei, Y. (2023). Efficient and cost-effective fl uorine recovery from liquid-phase wet-process phosphoric acid via two-ste p precipitation method. *Separation and Purification Technology*, *325*, 1246 87. https://doi.org/10.1016/j.seppur.2023.124687

He, C., Fang, K., Wang, W., Wang, Q., Luo, J., Ma, J., et al. (2022). Techno-eco nomic feasibility of “membrane-based pre-concentration + post-treatment” s ystems for municipal wastewater treatment and resource recovery. *Journal of Cleaner Production*, *375*, 134113. https://doi.org/10.1016/j.jclepro.2022.1 34113

Hu, R., Tian, Z., Fan, Z., Huang, T., & Wen, G. (2024). Pilot test on acidic fluor ide-containing wastewater treatment in the photovoltaic industry through in

554 duced crystallization with a focus on calcium fluoride recovery. *Separation*
555 *and Purification Technology*, *341*, 126879. https://doi.org/10.1016/j.seppur.
556 2024.126879
557 Hu, R., Yu, S., Fan, Z., Li, K., Huang, T., & Wen, G. (2025). Synergistic remova
558 l of fluoride, calcium, and manganese in composite polluted groundwater v
559 ia induced co-crystallization: effect and mechanism. *Journal of Environmen*
560 *tal Chemical Engineering*, *13*(5), 118905. https://doi.org/10.1016/j.jece.2025
561 .118905
562 Hu, W., Tang, Y., Wang, K., Xie, F., Wu, C., Li, W., et al. (2025). Rapid and dee
563 p removal of fluorine from wastewater by porous la-al layered double hyd
564 roxides material: reaction mechanism coupled with chemical precipitation a
565 nd adsorption. *Journal of Water Process Engineering*, *79*, 108997. https://d
566 oi.org/10.1016/j.jwpe.2025.108997
567 Huang, L., Yang, Z., He, Y., Chai, L., Yang, W., Deng, H., et al. (2020). Adsorpt
568 ion mechanism for removing different species of fluoride by designing of
569 core-shell boehmite. *Journal of Hazardous Materials*, *394*, 122555. https://
570 doi.org/10.1016/j.jhazmat.2020.122555
571 Jiang, K., Pan, X., Zhao, Z., Peng, Y., Cao, Z., & E, J. (2025). Simultaneous and
572 selective separation of fluorine and chlorine from zinc sulfate electrolyte
573 by nanofiltration membrane. *Desalination and Water Treatment*, *322*, 1010
574 80. https://doi.org/10.1016/j.dwt.2025.101080

Li, H., Chen, M., Ma, L., Wang, S., Liao, T., & Liu, Y. (2025). Breaking through the bottleneck of low-concentration fluoride treatment: action mechanisms, material design and practical applications of rare earth-doped hydroxyapatite. *Computational Materials Science*, *259*, 114159. https://doi.org/10.1016/j.commatsci.2025.114159

Lim, H. R., Choo, C. M., Chong, C. H., & Wong, V.-L. (2021). Optimization studies for water defluoridation with two-stage coagulation processes using new industrial-based chemical coagulants. *Journal of Water Process Engineering*, *42*, 102179. https://doi.org/10.1016/j.jwpe.2021.102179

Liu, D., Gong, J., Sun, C., Xu, L., & Song, Y. (2022). Enhanced photocatalytic activity for degradation of ofloxacin and dye by hierarchical flower-like ZnS/MoS2/Bi2WO6 heterojunction: synergetic effect of 2D/2D coupling interface and solid sulfide solutions. *Catalysis Communications*, *172*, 106546. https://doi.org/10.1016/j.catcom.2022.106546

Lv, S., Zhao, Y., Zhang, L., Zhang, T., Dong, G., Li, D., et al. (2023). Anion regulation strategy of lithium-aluminum layered double hydroxides for strengthening resistance to deactivation in lithium recovery from brines. *Chemical Engineering Journal*, *472*, 145026. https://doi.org/10.1016/j.cej.2023.145026

Meena, R. R., Singh, R. M., Soni, P., Kumar, R., & Kumar, S. (2024). Fluoride removal using a rotating anode electro-coagulation reactor: parametric opti

596 mization using response surface methodology, isotherms and kinetic studies
597 , economic analysis and sludge characterization. *Journal of Environmental*
598 *Management*, *370*, 122600. https://doi.org/10.1016/j.jenvman.2024.122600
599 Miao, Y., Gu, J., Zhu, D., Ye, C., Yang, Y., & Zhou, Q. (2025). Characterization
600 and performance of novel carbon-doped aluminum-modified bentonite for c
601 ost-effective fluoride removal. *Materials Today Communications*, *42*, 11115
602 6. https://doi.org/10.1016/j.mtcomm.2024.111156
603 Nazari, E., Rashchi, F., Saba, M., & Mirazimi, S. M. J. (2014). Simultaneous rec
604 overy of vanadium and nickel from power plant fly-ash: optimization of p
605 arameters using response surface methodology. *Waste Management*, *34*(12),
606 2687–2696. https://doi.org/10.1016/j.wasman.2014.08.021
607 Vasylyeva, H. V., Mironyuk, I. F., Mykytyn, I. M., Hnylytsia, I. D., & Vasyliev,
608 A. V. (2026). The influence of the TiO2 surfaces' chemosorbed fluorine at
609 oms on the adsorption of yttrium and zirconium cations. *Colloids and Surf*
610 *aces A: Physicochemical and Engineering Aspects*, *728*, 138539. https://doi
611 .org/10.1016/j.colsurfa.2025.138539
612 Wang, M., Luo, Y., Tuerhong, T., & Wang, Y. (2026). Adsorption of arsenic–fluor
613 ine in groundwater by fe/la-modified wheat straw–derived biochar. *Materia*
614 *ls Chemistry and Physics*, *348*, 131606. https://doi.org/10.1016/j.matchemp
615 hys.2025.131606
616 Wang, Q., Chen, P., Zeng, X., Jiang, H., Meng, F., Li, X., et al. (2020). Synthesis

of (ZrO2-Al2O3)/GO nanocomposite by sonochemical method and the me
chanism analysis of its high defluoridation. *Journal of Hazardous Material
s*, *381*, 120954. https://doi.org/10.1016/j.jhazmat.2019.120954

Wang, R., Zhang, C., Yu, H., & Sun, W. (2025). Research progress on hazardous
fluorine-containing wastewater treatment in the integrated circuit industry:
a resource recovery perspective. *Separation and Purification Technology*, *3
65*, 132626. https://doi.org/10.1016/j.seppur.2025.132626

Xia, Y., Ye, Y., Liu, M., Wang, Y., Shang, L., Wang, P., & Xu, Y. (2024). Effects
of high fluoride and iodine combined exposure on thyroid nodules and go
iter in school-age children in jiangsu, China. *Heliyon*, *10*(21), e40082. http
s://doi.org/10.1016/j.heliyon.2024.e40082

Yang, J., Gong, H., Chai, S., Zhu, D., Chen, K., Liu, Q., et al. (2025). Fluorine r
ecovery from low-concentration fluorine wastewater by flow-electrode capa
citive deionization and fluid bed crystallization (FCDI-FBC): preconcentrati
on and high-quality fluorite pellets formation. *Water Research*, *275*, 12322
8. https://doi.org/10.1016/j.watres.2025.123228

Zhang, Q., Shi, X., Wang, L., Li, Q., Xiong, R., Zhang, Z., et al. (2025). Regulat
ing crystal faces and pore size of layered double oxides for efficient phosp
horus recovery from water. *Journal of Water Process Engineering*, *75*, 108
033. https://doi.org/10.1016/j.jwpe.2025.108033

Zou, H., & Wang, Y. (2016). Phosphorus removal and recovery from domestic wa

638 stewater in a novel process of enhanced biological phosphorus removal co
639 upled with crystallization. *Bioresource Technology*, *211*, 87–92. https://doi.o
640 rg/10.1016/j.biortech.2016.03.073
641

Supplementary Files

This is a list of supplementary files associated with this preprint. Click to download.

- Supplementinformation.docx